Research Square

Preprints are preliminary reports that have not undergone peer review.
They should not be considered conclusive, used to inform clinical practice,
or referenced by the media as validated information.

Nicotinamide mononucleotide restores metabolic homeostasis in polyendocrine metabolic ovarian syndrome through the NAMPT/NAD$^+$/SIRT3 axis

Zhijing Na

sharon_na@foxmail.com

Shengjing Hospital of China Medical University

Fuyao Yang
Wanying Deng
Jiaye Pan
Yilin Li
Shuang Wei
Wenhui Gao
Shiqing Fan
Zhanao Liu
Yiwen Bao
Zhongxiu Jiang

Article

Keywords:

Posted Date: November 27th, 2026

DOI: https://doi.org/10.21203/rs.3.rs-10749025/v1

License: This work is licensed under a Creative Commons Attribution 4.0 International License.
Read Full License

Additional Declarations: There is **NO** conflict of interest to disclose

Nicotinamide mononucleotide restores metabolic homeostasis in polyendocrine metabolic ovarian syndrome through the NAMPT/NAD^+/SIRT3 axis

Fuyao Yang[1, †], Wanying Deng[2, †], Jiaye Pan[2, †], Yilin Li[1, †], Shuang Wei[1], Wenhui Gao[1], Shiqing Fan[5], Zhanao Liu[1], Yiwen Bao[2, 4, *], Zhongxiu Jiang[2, *], Zhijing Na[1, 3, *]

[1]Center of Reproductive Medicine, Department of Obstetrics and Gynecology, Shengjing Hospital of China Medical University, Shenyang, China

[2]Department of Obstetrics and Gynecology, Shengjing Hospital of China Medical University, Shenyang, China

[3]NHC Key Laboratory of Advanced Reproductive Medicine and Fertility (China Medical University), National Health Commission, Shenyang, China

[4]Department of Biobank, Shengjing Hospital of China Medical University, Shenyang, Liaoning, China

[5]Department of Blood Transfusion, Shengjing Hospital of China Medical University, Shenyang, Liaoning, China

[†]These authors contributed equally to this work.

[*]**Corresponding authors:**

Zhijing Na, MD, PhD, Email: sharon_na@foxmail.com.

Zhongxiu Jiang, MD, PhD, Email: jiangzhx1986@163.com.

Yiwen Bao, MD, PhD, Email: baoyw@sj-hospital.org.

Running Title: NMN Restores Ovarian Function in PMOS

Abstract

Background

Polyendocrine metabolic ovarian syndrome (PMOS, formerly known as polycystic ovary syndrome) involves both reproductive dysfunction and metabolic disturbances, including insulin resistance and hyperandrogenism. Mitochondrial impairment in granulosa cells may participate in ovarian dysfunction, although the metabolic regulation of mitochondrial quality control in PMOS remains incompletely understood. Therefore, we examined whether NAMPT-dependent NAD^+ metabolism and SIRT3 signaling contribute to mitochondrial homeostasis, and whether nicotinamide mononucleotide (NMN) can counteract PMOS-associated abnormalities.

Methods

Follicular fluid-derived single-cell RNA-sequencing data from women with PMOS and controls were reanalyzed (n = 3 per group). Three experimental groups of mice were established: control, PMOS, and PMOS plus NMN (n = 9 per group). PMOS was induced with DHT, and NMN was administered intraperitoneally at 500 mg/kg/day for 21 days. In parallel, KGN and COV434 granulosa-like cells were exposed to DHT (1 μM, 48 h), either alone or combination with NMN (500 μM, 48 h).

Results

Single-cell analysis revealed transcriptional remodeling of granulosa cells in patients with PMOS, including altered insulin-response pathways. DHT-induced PMOS ovaries and DHT-exposed granulosa-like cells showed elevated NAMPT expression despite reduced NAD^+ availability and diminished SIRT3 signaling. Additionally, there were

increased PINK1/Parkin-associated mitophagy markers. Loss of NAMPT aggravated mitochondrial abnormalities, whereas NAMPT overexpression exerted a protective effect. NMN replenished intracellular NAD^+, recovered SIRT3 signaling, attenuated mitophagy-related changes, preserved mitochondrial membrane potential, and limited mitochondrial reactive oxygen species accumulation. In PMOS mice, NMN improved responses to glucose and insulin challenges, reduced hyperandrogenemia, partially restored estrous cyclicity, and ameliorated ovarian morphological and follicular abnormalities.

Conclusions

These findings identify the NAMPT/NAD^+/SIRT3 axis as a metabolic link between PMOS and granulosa cell mitochondrial dysfunction. Restoring NAD^+ availability with NMN produced both mitochondrial and ovarian benefits in preclinical models, supporting further translational evaluation of NAD^+ repletion as a potential intervention for PMOS.

Keywords: Polyendocrine metabolic ovarian syndrome; Nicotinamide mononucleotide; NAD^+ metabolism; Mitophagy

1. Introduction

Polyendocrine metabolic ovarian syndrome (PMOS, formerly polycystic ovary syndrome) is a common reproductive and metabolic disorder characterized by hyperandrogenism, ovulatory dysfunction, and metabolic abnormalities [1-3]. Granulosa cells (GCs) provide metabolic and paracrine support for oocyte maturation and follicular development, and may therefore link systemic metabolic disturbances to local ovarian dysfunction [4-7]. Mitochondrial homeostasis is essential for GC function, whereas oxidative and metabolic stress in PMOS can impair mitochondrial integrity and follicular development [8-10]. Mitophagy contributes to mitochondrial quality control by removing damaged mitochondria; however, dysregulated mitophagy may aggravate GC dysfunction [9, 11-14]. The mechanisms linking PMOS-associated metabolic disturbances to altered mitophagy in GCs remain unclear.

Nicotinamide adenine dinucleotide (NAD^+) is a central coenzyme in cellular energy metabolism and mitochondrial homeostasis. Nicotinamide mononucleotide (NMN), a naturally occurring NAD^+ intermediate, can replenish intracellular NAD^+ and has attracted interest as a bioactive NAD^+ precursor [15-17]. In preclinical studies, NAD^+-precursor supplementation has improved ovarian or metabolic abnormalities and reduced mitochondrial and inflammatory stress [18-20]. NAD^+ homeostasis is maintained predominantly through the nicotinamide phosphoribosyltransferase (NAMPT)-dependent salvage pathway. NAD^+ availability also supports the activity of the mitochondrial deacetylase sirtuin 3 (SIRT3), which regulates mitochondrial metabolism and quality control [21-24]. Although NMN has shown metabolic and

mitochondrial benefits in several disease models [15, 25, 26], whether it modulates GC mitochondrial quality control in PMOS through the NAMPT/NAD^+/SIRT3 axis remains unclear.

Therefore, we investigated the relationship between NAMPT-mediated NAD^+ metabolism, SIRT3 signaling, and mitophagy-related abnormalities in PMOS GCs. Using single-cell transcriptomic analysis, hyperandrogenic granulosa-like cell models, and a dihydrotestosterone (DHT)-induced PMOS mouse model, we further examined whether NMN administration restores mitochondrial homeostasis and improves metabolic and ovarian phenotypes. This study was designed to define the metabolic mechanisms underlying GC dysfunction in PMOS and to assess the preclinical potential of NAD^+ repletion.

2. Methods

2.1. Bioinformatics analysis

2.1.1. Data collection and preprocessing

Single-cell RNA-sequencing data from GSE240688, comprising follicular fluid samples from three patients with PMOS and three control individuals, were retrieved from the Gene Expression Omnibus (GEO; https://www.ncbi.nlm.nih.gov/gds) and initially processed using the standard BD pipeline. Subsequent quality control and data processing were conducted in Seurat. Cells were excluded if they contained fewer than 500 unique molecular identifier (UMI) counts, had nFeature_RNA values above the 97th percentile, or showed mitochondrial gene expression exceeding 20% of total

expression. Following quality filtering, expression values were normalized with NormalizeData, and the top 2,000 highly variable genes were selected with FindVariableFeatures. ScaleData was then applied while regressing out mitochondrial gene percentage together with S- and G2/M-phase scores. The processed dataset was subjected to principal component analysis (PCA), followed by nearest-neighbor graph construction, clustering, and uniform manifold approximation and projection (UMAP). Putative doublets were subsequently detected and excluded using scDblFinder.

2.1.2. Differential expression and gene set enrichment analysis

Data from the six samples were first combined with JoinLayers, after which batch-associated variation was corrected using Harmony (v1.2.3). The Harmony-corrected embeddings were used for subsequent clustering and UMAP visualization. Cluster-enriched genes were identified with FindMarkers, and cell identities were assigned according to canonical marker expression. For GC pseudo-bulk analysis, raw counts were summed at the sample level before differential expression analysis with limma. Genes were subsequently ordered according to their t-statistics and subjected to gene set enrichment analysis using fgsea. Enrichment was evaluated for NR0B1_TARGET_GENES and GOBP_RESPONSE_TO_INSULIN, with gene sets meeting $P < 0.05$ and $NES > 1.3$ regarded as significantly enriched.

2.2. PMOS mouse model

Female C57BL/6J mice aged 3 weeks were obtained from Beijing HFK Bioscience Co.,

Ltd. (Beijing, China) and maintained under specific-pathogen-free conditions. Following a 3-day acclimation period, animals were randomized into control, dihydrotestosterone (DHT; GlpBio, Montclair, CA, USA; GC19064)-induced PMOS, and DHT plus NMN (APExBIO, Houston, TX, USA; B7878) groups (n = 9 per group). PMOS was established using a modified version of our previously reported protocol [27], with DHT administered subcutaneously in sesame oil at 6 mg/100 g body weight once daily for 21 days. During the same 21-day period, mice assigned to NMN treatment received 500 mg/kg NMN intraperitoneally each day, while control and PMOS animals received volume-matched saline. Dosages were adjusted according to individual body weight [17]. Estrous cyclicity was monitored by daily vaginal cytology beginning on day 12. All procedures were approved by the Animal Care and Use Committee of Shengjing Hospital of China Medical University (2025PS062K(X1)) and conducted in accordance with the National Institutes of Health Guide for the Care and Use of Laboratory Animals.

2.3. Assessment of PMOS-related phenotypes

2.3.1 Glucose tolerance test and Insulin tolerance test

Glucose tolerance was evaluated after a 14-h fasting period. Mice received glucose intraperitoneally at 2 g/kg, and glycemia was recorded before injection and at 15, 30, 60, 90, and 120 min thereafter. Insulin sensitivity was assessed separately following 6 hs of fasting by administering insulin at 0.5 IU/kg, with glucose measurements obtained at baseline and 15, 30, 45, and 60 min after injection. GraphPad Prism 9 was used to

calculate the corresponding areas under the glucose curves (AUCs).

2.3.2. Enzyme-linked immunosorbent assay (ELISA)

Under anesthesia, blood samples were obtained from the retro-orbital venous plexus and processed by centrifugation at 2,800 × g for 10 min at 4 ℃. The isolated serum was maintained at −80 ℃ before measurement of FSH, LH, and testosterone using commercial ELISA kits (Solarbio; SEKM-0251, SEKM-0252, and SEKSM-0030, respectively).

2.3.3. Hematoxylin and eosin staining (H&E)

For histological evaluation, ovaries were preserved in 4 % paraformaldehyde and subsequently processed for paraffin embedding. Sections with a 5 μm thickness were prepared and subjected to H&E staining.

2.4. Cell culture and treatment

KGN and COV434 human granulosa-like tumor cells were obtained from Suzhou Haixing Biosciences Co., Ltd. (Suzhou, China). KGN cells were maintained in Dulbecco's modified Eagle's medium (DMEM; Gibco, Grand Island, NY, USA), whereas COV434 cells were maintained in RPMI 1640 (Gibco); both media contained 10% fetal bovine serum and 1% penicillin–streptomycin (Gibco). Cultures were kept at 37 ℃ in a humidified 5 % CO_2 atmosphere. A hyperandrogenic condition was generated by exposing cells to 1 μM DHT for 48 h according to the reported protocol [28]. Where indicated, NMN was administered at 500 μM for 48 h. Vehicle-matched controls

received ethanol for DHT or sterile double-distilled water for NMN.

2.5. siRNA transfection and plasmid-mediated overexpression

KGN and COV434 cells were plated in six-well plates and used for transfection once approximately 60 %–70 % confluence was reached. Lipofectamine 3000 (Thermo Fisher Scientific, Waltham, MA, USA; L3000015) served as the transfection reagent. NAMPT-targeting siRNA was tested at final concentrations of 75 nM and 100 nM, with the latter concentration used in subsequent experiments due to its greater knockdown efficiency. SIRT3-targeting siRNA and the non-targeting negative control siRNA (si-NC) were each applied at 75 nM. All siRNAs were purchased from General Biosystems Co., Ltd. (Chuzhou, China), with sequences listed in **Supplementary Table S1**.

For gain-of-function experiments, 2.5 μg of the NAMPT expression plasmid or its corresponding empty vector (OE-NC) was introduced into cells with Lipofectamine 3000 and P3000 reagent. Plasmids were supplied by Shenyang Mingsheng Biotechnology Co., Ltd. (Shenyang, China). Culture medium was renewed 6–8 h after transfection, and cells were collected 24–48 h later. Transfection efficiency was assessed by reverse transcription quantitative polymerase chain reaction (RT-qPCR) and/or western blotting.

2.6. RNA extraction and RT-qPCR

RNA isolated from ovarian tissues and cultured cells with a commercial kit (TaKaRa, Kusatsu, Shiga, Japan; 9109) was evaluated spectrophotometrically before cDNA

synthesis; only preparations with A_{260}/A_{280} values between 1.8 and 2.0 were used. RT-qPCR was carried out with TB Green Premix Ex Taq (TaKaRa; RR420A) on a QuantStudio 5 system (Applied Biosystems, Foster City, CA, USA), and product specificity was verified by melting curves analysis. *ACTB/Actb* was used for normalization except when mouse ovarian *Nampt* was analyzed, in which case *Gapdh* served as the reference. Fold changes were caculated using the 2^−ΔΔCt method. Primer information is listed in **Supplementary Table S2**.

2.7. Western blot

Proteins were extracted from cultured cells or ovarian tissues in RIPA buffer (KeyGEN, Nanjing, China; KGB5203-100) containing protease and phosphatase inhibitors and quantified by BCA assay (SevenBio, Beijing, China; SW201-02). For each sample, 20 μg of protein was resolved by 10 % SDS-PAGE and transferred onto PVDF membranes (Millipore, Burlington, MA, USA). After blocking in 5 % non-fat milk, membranes were probed at 4 ℃ overnight with antibodies against NAMPT, SIRT3, Pink1, Parkin, LC3B, Beclin1, or p62. HRP-conjugated secondary antibodies were subsequently applied for 1 h at room temperature. Immunoreactive bands were detected by enhanced chemiluminescence and analyzed densitometrically in ImageJ. HSP90 or β-tubulin served as loading controls, and LC3B processing was evaluated using the LC3B-II/LC3B-I ratio. Antibody information is listed in **Supplementary Table S3**.

2.8. NAD^+ and NADH assay

Ovarian and cellular NAD^+/NADH contents were quantified using a commercial colorimetric assay (Elabscience Biotechnology; E-BC-K804-M). Ovarian samples were extracted in ice-cold buffer and clarified by centrifugation at 10,000 × g for 10 min at 4 ℃. For cultured cells, approximately 1.5×10^6 cells were suspended in 0.4 mL of extraction buffer, followed by centrifugation at 12,000 × g for 10 min at 4 °C. Total NAD was determined without additional treatment, whereas NADH was quantified after aliquots had been heated at 60 ℃ for 30 min to remove NAD^+. Absorbance was recorded at 450 nm according to the kit protocol. NAD^+ was obtained by subtracting NADH from total NAD, after which the NAD^+/NADH ratio was calculated.

2.9. Assessment of mitochondrial membrane potential and mitochondrial reactive oxygen species

Mitochondrial membrane potential and mitochondrial ROS were assessed using Tetramethylrhodamine ethyl ester perchlorate (TMRE; MedChemExpress, Monmouth Junction, NJ, USA; HY-D0985A) and MitoSOX Red (MedChemExpress; HY-D1055), respectively. Each probe was prepared as a 5 mM DMSO stock solution and diluted in serum-free medium to 10 μM before use. Following experimental treatment, cells were loaded with the corresponding dye for 30 min at 37 ℃ in the dark, then washed and counterstained with Hoechst. Fluorescence images were collected with a Nikon A1 confocal microscope (Nikon, Tokyo, Japan). ImageJ-based fluorescence measurements were normalized to the number of Hoechst-positive nuclei; TMRE intensity was used as an index of membrane potential, whereas MitoSOX Red intensity reflected

mitochondrial ROS production.

2.10. Immunofluorescence and immunohistochemistry

2.10.1 Immunofluorescence staining

Immunofluorescence was performed on cells cultured on glass coverslips. Following fixation in 4 % paraformaldehyde, cells were permeabilized with 0.2 % Triton X-100 and subjected to blocking with 5 % bovine serum albumin. Primary labeling for TOMM20 or LC3B was carried out overnight at 4 ℃, after which appropriate fluorophore-labeled secondary antibodies were applied for 1 h at room temperature. DAPI or Hoechst was used for nuclear counterstaining. All groups were imaged using the same acquisition parameters. Quantification was performed in ImageJ; mitochondrial abundance was assessed from TOMM20 fluorescence intensity, whereas LC3B accumulation was determined from LC3B-positive puncta or stained area.

2.10.2 Immunohistochemistry

Ovarian samples embedded in paraffin were sectioned at a thickness of 5 μm for immunohistochemical assessment with a kit (KeyGEN; KGC3201-300). Sections were sequentially deparaffinized, rehydrated, subjected to antigen retrieval, and blocked before incubation with antibodies recognizing NAMPT, Beclin1, or Pink1 at 4 ℃ overnight. Antibody binding was visualized using 3,3′-diaminobenzidine, and hematoxylin was subsequently used to counterstain nuclei. Imaging parameters were kept constant across experimental groups. Quantification was based on five randomly

selected, non-overlapping fields per sample at ×20 magnification. ImageJ was used to determine the average optical density in each field, after which the five measurements were averaged to generate a single value for each biological replicate.

2.11. Statistical analysis

GraphPad Prism 9 was used for all statistical evaluations. Unless stated otherwise, results are expressed as mean ± SD, and in vitro experiments were performed in at least three independent replicates. For comparisons between two independent groups, a two-tailed unpaired Student's t-test was applied, with Welch's adjustment used when variance homogeneity was not met. Datasets involving three or more groups were evaluated by one-way ANOVA followed by Tukey's multiple comparisons procedure. Time-dependent GTT and ITT measurements were analyzed by two-way ANOVA, while their corresponding AUCs were assessed using either a t-test or one-way ANOVA, as appropriate. Statistical significance was accepted at $P < 0.05$.

3. Results

3.1. Single-Cell Transcriptomic Remodeling in Ovarian GCs from PMOS Patients

Using the GSE240688 dataset, we analyzed scRNA-seq data from follicular fluid-derived cells of three PMOS patients and three controls. After normalization, dimensionality reduction, and clustering, nine major cell clusters (Clusters 0–8) displaying substantial transcriptional heterogeneity were identified **(Fig. 1A)**. Cluster 8 showed high expression of the proliferation markers MKI67 and PCNA, whereas

Cluster 5 exhibited a p53-stress signature **(Fig. 1B)**. Marker-based annotation identified normal, proliferative, and p53-stressed GC populations, as well as immune populations, including neutrophils, dendritic cells, and monocytes/macrophages **(Fig. 1C, D)**. GSEA of pseudo-bulked GC expression showed significant enrichment of NR0B1_TARGET_GENES and GOBP_RESPONSE_TO_INSULIN in PMOS, with partial overlap **(Fig. 1E–G)**. Together, these results indicate transcriptomic remodeling in PMOS GCs, including altered proliferative/stress states and insulin responses.

3.2. DHT-induced PMOS mice display metabolic disorders and ovarian mitophagy-related abnormalities

Vaginal cytology and H&E staining revealed disrupted estrous cycles, enlarged cystic follicles, thinning of the GC layer, and reduced corpus luteum formation in PMOS mice **(Fig. 2A, D, E)**. GTT and ITT showed elevated fasting blood glucose and AUCs, indicating impaired glucose tolerance and insulin resistance **(Fig. 2B, C)**. Immunohistochemistry and Western blotting showed increased Beclin1 and Pink1 expression in ovarian tissues from PMOS mice **(Fig. 2F–I)**. RT-qPCR and Western blotting further showed increased LC3B-II, Pink1, and Parkin protein levels, as well as increased LC3B, Pink1, Parkin, and Beclin1 transcripts, whereas p62 protein remained unchanged despite reduced mRNA expression **(Fig. 2H, I and Fig. S1A–E)**. These findings indicate systemic metabolic dysfunction accompanied by activation of ovarian Pink1/Parkin-related mitophagy signaling.

3.3. NAMPT maintains NAD^+ homeostasis and mitochondrial integrity in the cell model of PMOS

Given the mitochondrial abnormalities observed in PMOS ovaries, we next sought to identify metabolic regulators associated with GC mitochondrial homeostasis. Pseudo-bulk analysis of GC transcriptomes from PMOS patients revealed altered expression of NAMPT and several metabolism-related genes, including *IRS2*, *PIK3R1*, and *NCOA2* **(Fig. 3A)**, suggesting a potential involvement of NAMPT in PMOS-associated metabolic remodeling. Consistent with the transcriptomic findings, immunohistochemical staining, Western blotting, and RT-qPCR analyses demonstrated increased NAMPT expression in ovarian tissues from PMOS mice **(Fig. 3B–E)**. However, metabolite profiling revealed that NAMPT upregulation was not sufficient to preserve NAD^+ homeostasis. PMOS ovaries exhibited decreased NAD^+ levels, increased NADH accumulation, and a markedly reduced NAD^+/NADH ratio **(Fig. 3F–H)**. In vitro, DHT exposure to mimic the hyperandrogenic PMOS environment similarly increased NAMPT expression in GCs **(Fig. 3I and Fig. S2A)**, accompanied by reduced intracellular NAD^+ availability and a decreased NAD^+/NADH ratio **(Fig. S2B–D)**. To determine whether NAMPT directly regulates mitochondrial homeostasis, NAMPT expression was experimentally manipulated in GCs. NAMPT knockdown resulted in reduced TOMM20 fluorescence intensity, decreased mitochondrial membrane potential as assessed by TMRE staining, increased mitochondrial ROS accumulation detected by MitoSOX Red staining, and enhanced punctate LC3 aggregation, indicating impaired mitochondrial quality control. Conversely, NAMPT

overexpression reversed these mitochondrial abnormalities **(Fig. 3J–O)**. Collectively, these findings indicate that NAMPT serves as an important regulator of NAD^+ metabolic homeostasis and mitochondrial integrity in GCs. However, the mechanisms linking NAMPT-mediated NAD^+ metabolism to mitochondrial quality control remain unclear, prompting further investigation into NAD^+-dependent signaling pathways.

3.4. NAMPT maintains mitochondrial homeostasis through the NAD^+/SIRT3 signaling axis in GCs

To investigate the molecular mechanism linking NAMPT-mediated NAD^+ metabolism to mitochondrial quality control, we focused on the NAD^+-dependent deacetylase SIRT3. Western blotting and RT-qPCR analyses demonstrated that NAMPT knockdown significantly reduced SIRT3 protein and *SIRT3* mRNA expression, whereas NAMPT overexpression increased SIRT3 expression **(Fig. 4A, B)**, indicating that NAMPT positively regulates SIRT3 expression in GCs. To further determine the functional role of SIRT3, we examined mitophagy-related signaling following SIRT3 depletion. SIRT3 knockdown increased the protein levels of Pink1 and Parkin and elevated the LC3B-II/LC3B-I ratio, accompanied by altered p62 expression **(Fig. 4E, F)**, suggesting enhanced activation of mitophagy-associated pathways. Consistent with these molecular changes, SIRT3 deficiency resulted in impaired mitochondrial homeostasis, characterized by reduced TOMM20 fluorescence intensity, decreased mitochondrial membrane potential as assessed by TMRE staining, and increased mitochondrial ROS accumulation detected by MitoSOX Red staining **(Fig. 4G–L)**.

Together, these findings demonstrate that NAMPT regulates mitochondrial quality control through the NAD^+/SIRT3 signaling axis, and that disruption of SIRT3 activity promotes mitochondrial dysfunction and activation of mitophagy-related signaling in GCs.

3.5. NMN supplementation restores NAD^+/SIRT3 signaling and ameliorates PMOS-associated mitochondrial dysfunction in GCs

To determine whether restoration of NAD^+ availability could reverse NAMPT deficiency-induced mitochondrial abnormalities, GCs with NAMPT knockdown were treated with the NAD^+ precursor NMN. Biochemical analysis demonstrated that NMN supplementation significantly restored intracellular NAD^+ levels and improved the NAD^+/NADH ratio in NAMPT-deficient cells **(Fig. 5A–C)**. Consistently, NMN treatment reduced mitophagy-related abnormalities induced by NAMPT deficiency, as indicated by decreased Pink1 and Parkin protein expression and restoration of the LC3B-II/LC3B-I ratio **(Fig. 5D–H)**. Immunofluorescence analysis further demonstrated that NMN restored TOMM20 fluorescence intensity, reduced LC3 puncta accumulation, improved mitochondrial membrane potential assessed by TMRE staining, and decreased mitochondrial ROS production detected by MitoSOX Red staining **(Fig. 5L–Q)**. To further validate the protective effect of NMN under hyperandrogenic conditions, GCs were exposed to DHT with or without NMN supplementation. DHT treatment significantly reduced SIRT3 protein and *SIRT3* mRNA expression, whereas NMN supplementation restored SIRT3 expression **(Fig.**

5I–K). In parallel, DHT exposure induced mitochondrial loss and excessive mitophagy-related changes, characterized by reduced TOMM20 fluorescence intensity and increased LC3 puncta formation, which were partially reversed by NMN treatment **(Fig. S3A–C)**. Functional mitochondrial assays further showed that NMN rescued DHT-induced mitochondrial membrane potential loss and reduced mitochondrial ROS accumulation **(Fig. S3D–F)**.

3.6. NMN Administration Ameliorates Ovarian Dysfunction in a PMOS Mouse Model

Building on the in vitro mechanisms, we evaluated the therapeutic potential of intraperitoneally administered NMN in DHT-induced PMOS mice **(Fig. 6A)**. Intraperitoneal administration of NMN for 21 consecutive days significantly improved glucose metabolic abnormalities, as evidenced by markedly reduced AUCs in GTT and ITT curves **(Fig. 6B–E)**. Histopathological analysis revealed that NMN treatment reduced the number of cystic follicles, increased GC layers, and improved overall follicular development and ovarian architecture **(Fig. 6F)**. Furthermore, NMN intervention partially restored the disrupted estrous cycles **(Fig. 6G)**. Notably, serum hormone profiling showed that NMN significantly reduced elevated levels of luteinizing hormone (LH), the LH/FSH ratio, and testosterone in PMOS mice **(Fig. 6H)**. At the ovarian metabolic level, NMN supplementation effectively corrected the NAD^+/NADH redox imbalance by reducing elevated NADH levels, with a trend toward restoring NAD^+ levels **(Fig. 6I)**. Mechanistically, NMN intervention reduced the

protein levels of Beclin1, NAMPT, Parkin, Pink1, LC3B-I, and LC3B-II, while increasing p62 and SIRT3 protein expression. NMN also regulated the corresponding transcript levels in ovarian tissue **(Fig. 6J–M)**. In conclusion, NMN administration remodels GC mitochondrial homeostasis by restoring the NAMPT/NAD^+/SIRT3 axis, thereby systemically improving the metabolic and reproductive-endocrine disturbances characteristic of PMOS.

4. Discussion

This study provides mechanistic evidence that NMN administration restores ovarian function and metabolic homeostasis in a PMOS model. It achieves this by correcting the dysregulated NAMPT/NAD^+/SIRT3 axis and suppressing excessive Pink1/Parkin-mediated mitophagy in GCs. These findings highlight the potential of food-derived NAD^+ precursors for managing reproductive-metabolic disorders, offering a nutritional alternative to conventional hormone therapies.

We identified a distinct compensatory imbalance in PMOS GCs characterized by high NAMPT expression yet paradoxically low NAD^+ levels. While hyperandrogenic conditions induced NAMPT upregulation, the NAD^+/NADH ratio remained significantly depressed, indicating that endogenous NAMPT-mediated NAD^+ salvage is insufficient to counteract PMOS-related NAD^+ depletion. Exogenous NMN restored NAD^+ levels and enhanced SIRT3 signaling, thereby attenuating excessive mitophagy. Although these results align with recent studies on NAD^+ precursors improving oocyte quality [9, 18, 29], our work specifically pinpoints GC mitochondrial quality control as

413 the primary mechanism. We demonstrate that NMN administration reverses overactive
414 autophagy by re-establishing NAD^+/SIRT3 homeostasis, providing a mechanistic basis
415 for nutritional interventions in reproductive metabolic diseases.

416 Functional assays further supported a protective, albeit inadequate, compensatory
417 role for NAMPT in PMOS. NAMPT knockdown exacerbated NAD^+/NADH depletion
418 and SIRT3 downregulation, increased mitochondrial ROS accumulation, and altered
419 mitophagy-related signaling. Conversely, NMN supplementation or NAMPT
420 overexpression restored mitochondrial stability. This suggests that, while the body
421 attempts to compensate via NAMPT upregulation, it cannot offset the persistent NAD^+
422 consumption and redox stress in PMOS. Exogenous NMN bypasses this bottleneck by
423 restoring the NAD^+/SIRT3 signaling axis and modulating mitophagy-related signaling.
424 Notably, restoring SIRT3, a key mitochondrial deacetylase [30-32], not only improves
425 oxidative metabolism but may also restore balanced Pink1/Parkin-mediated mitophagy
426 by regulating mitochondrial quality control pathways [33-35].

427 Mitophagy in PMOS GCs exhibits a context-dependent role: physiological
428 mitophagy maintains mitochondrial homeostasis, whereas chronic hyperandrogenic
429 stress may induce excessive mitophagic activity, leading to impaired mitochondrial
430 quality and compromised bioenergetic capacity during follicular development [12, 36].
431 Unlike synthetic interventions that often target individual molecular nodes, NMN
432 administration may not function as a simple activator or inhibitor of autophagy. Instead,
433 by restoring NAD^+/SIRT3 signaling, NMN may help re-establish mitophagic
434 homeostasis and preserve mitochondrial quality control under pathological conditions

435 [37-39]. This systems-level mechanism supports the potential application of NMN as a
436 functional food-derived intervention.

437 Current nutritional strategies for PMOS largely involve bioactive compounds such
438 as polyphenols and fatty acids. Polyphenols have been reported to regulate metabolic
439 pathways, including AMPK/SIRT1 signaling, contributing to improvements in insulin
440 resistance and hyperandrogenic features, whereas fatty acid-based interventions mainly
441 exert anti-inflammatory and lipid-modulating effects. However, their clinical
442 translation remains limited by issues including variable bioavailability, heterogeneous
443 responses, and inconsistent phenotypic outcomes [40-43]. In contrast, NMN represents
444 a unique nutritional strategy by replenishing NAD^+ availability rather than targeting a
445 single downstream pathway. Restoration of NAD^+ homeostasis by NMN improves
446 systemic metabolic function and reproductive phenotypes, including recovery of
447 estrous cyclicity, enhanced insulin sensitivity, and attenuation of oxidative stress in
448 PMOS-related and metabolic models [44-47]. Furthermore, the favorable safety profile
449 of NMN supplementation reported in current studies supports its potential application
450 in functional food development. Challenges remain, however, including phenotypic
451 variability in treatment response, optimal dosing, long-term safety, and potential
452 synergies with other dietary actives. Future validation through human cohorts and
453 diverse animal models is warranted.

454 In conclusion, by introducing NMN administration into the study of GC
455 mitochondrial quality control, this research demonstrates that restoring NAD^+/SIRT3
456 homeostasis can normalize excessive mitophagic activity, thereby ameliorating ovarian

dysfunction and metabolic disturbances. Our findings support further evaluation of NMN as a candidate metabolic intervention for PMOS-related ovarian and metabolic dysfunction.

5. Conclusions

In summary, this study reveals that NAD^+ deficiency-associated disruption of mitochondrial quality control is a key metabolic mechanism contributing to PMOS-associated ovarian dysfunction. We identify the NAMPT/NAD^+/SIRT3 axis as a critical regulator linking metabolic imbalance to Pink1/Parkin-mediated mitophagy dysregulation in GCs. NMN supplementation restores NAD^+ homeostasis, reactivates SIRT3-mediated mitochondrial protection, and reverses PMOS-associated ovarian dysfunction and metabolic abnormalities. Our findings provide a mechanistic rationale for targeting NAD^+ metabolism as a promising nutritional and therapeutic strategy to preserve ovarian function in PMOS.

Declarations

Ethics approval and consent to participate

The ethics application was approved by the Ethics Committee of Shengjing Hospital of China Medical University (Approval No. 2025PS062K(X1)).

Availability of data and materials

The original data presented in the study are included in the article. Further inquiries can be directed to the corresponding authors.

Declaration of competing interest

The authors declare no competing interests.

Funding

This work was supported by the National Key Research and Development Program (No. 2024YFC2706900); National Natural Science Foundation grant of China (No. 82401928).

Authors' contributions

Fuyao Yang, Wanying Deng, Jiaye Pan, Yilin Li: Writing – original draft, Visualization, Validation, Software, Methodology, Investigation, Formal analysis. Shuang Wei: Formal analysis. Wenhui Gao: Data curation. Shiqing Fan: Data curation. Zhanao Liu: Data curation. Zhijing Na, Zhongxiu Jiang, Yiwen Bao: Writing – review & editing, Supervision, Project administration, Funding acquisition.

References

1. Teede HJ, Tay CT, Laven J, Dokras A, Moran LJ, Piltonen TT, et al. Recommendations from the 2023 international evidence-based guideline for the assessment and management of polycystic ovary syndrome. Hum Reprod. 2023;38:1655–79.

2. Kim KW. Unravelling polycystic ovary syndrome and its comorbidities. J Obes Metab Syndr. 2021;30:209–21.

3. Joham AE, Norman RJ, Stener-Victorin E, Legro RS, Franks S, Moran LJ, et al. Polycystic ovary syndrome. Lancet Diabetes Endocrinol. 2022;10:668–80.

4. Zhang CH, Liu XY, Wang J. Essential role of granulosa cell glucose and lipid metabolism on oocytes and the potential metabolic imbalance in polycystic ovary syndrome. Int J Mol Sci. 2023;24:16247.

5. Richani D, Dunning KR, Thompson JG, Gilchrist RB. Metabolic co-dependence of the oocyte and cumulus cells: Essential role in determining oocyte developmental competence. Hum Reprod Update. 2021;27:27–47.

6. Morimoto A, Rose RD, Smith KM, Dinh DT, Umehara T, Winstanley YE, et al. Granulosa cell metabolism at ovulation correlates with oocyte competence and is disrupted by obesity and aging. Hum Reprod. 2024;39:2053–66.

7. Li Q, Sang Y, Chen Q, Ye B, Zhou X, Zhu Y. Integrated bioinformatics analysis elucidates granulosa cell whole-transcriptome landscape of PCOS in China. J Ovarian Res. 2023;16:154.

8. Gao Y, Zou Y, Wu G, Zheng L. Oxidative stress and mitochondrial dysfunction of granulosa cells in polycystic ovarian syndrome. Front Med (Lausanne). 2023;10:1193749.

9. Zhang Q, Ren J, Wang F, Pan M, Cui L, Li M, et al. Mitochondrial and glucose metabolic dysfunctions in granulosa cells induce impaired oocytes of polycystic ovary syndrome through sirtuin 3. Free Radic Biol Med. 2022;187:1–16.

10. Xie C, Lu H, Zhang X, An Z, Chen T, Yu W, et al. Mitochondrial abnormality in ovarian granulosa cells of patients with polycystic ovary syndrome. Mol Med Rep. 2024;29:27.

11. Li A, Gao M, Liu B, Qin Y, Chen L, Liu H, et al. Mitochondrial autophagy: Molecular mechanisms and implications for cardiovascular disease. Cell Death Dis. 2022;13:444.

12. Yi S, Zheng B, Zhu Y, Cai Y, Sun H, Zhou J. Melatonin ameliorates excessive PINK1/Parkin-mediated mitophagy by enhancing SIRT1 expression in granulosa cells of PCOS. Am J Physiol Endocrinol Metab. 2020;319:E91–E101.

13. Xie C, Liu Z, Chen T, Lu H, Zhang X, Yu W, et al. Melatonin alleviates mitochondrial damage by regulating SIRT3-mediated mitochondrial dynamics in granulosa cells under PCOS-like conditions. Mol Med Rep. 2026;34:227.

14. Tian Y, Pan P, Luo X, Sun Y, Yang X, Gao H, et al. Palmitic acid-induced insulin resistance triggers granulosa cell senescence by disruption of the UPR(mt)/mitophagy/lysosome axis. Chem Biol Interact. 2025;411:111450.

15. Mills KF, Yoshida S, Stein LR, Grozio A, Kubota S, Sasaki Y, et al. Long-term administration of nicotinamide mononucleotide mitigates age-associated physiological decline in mice. Cell Metab. 2016;24:795–806.

16. Alegre GFS, Pastore GM. NAD^+ precursors nicotinamide mononucleotide (NMN) and nicotinamide riboside (NR): Potential dietary contribution to health. Curr Nutr Rep. 2023;12:445–64.

17. Liang J, Huang F, Hao X, Zhang P, Chen R. Nicotinamide mononucleotide supplementation rescues mitochondrial and energy metabolism functions and ameliorates inflammatory states in the ovaries of aging mice. MedComm (2020). 2024;5:e727.

18. Zhu Z, Lei M, Guo R, Xu Y, Zhao Y, Wei C, et al. Nicotinamide riboside supplementation ameliorates ovarian dysfunction in a PCOS mouse model. J Ovarian Res. 2025;18:9.

19. Yang X, Huang K, Qin J, Cui X, Zhang Z, Huang Q, et al. NAD^+ rescues phosphatidylinositol-induced granulosa cell pyroptosis to restore follicular development in PCOS. Free Radic Biol Med. 2025;241:287–98.

20. Ahmed M, Riaz U, Lv H, Amjad M, Ahmed S, Ali S, et al. Nicotinamide mononucleotide restores NAD^+ levels to alleviate LPS-induced inflammation via the TLR4/Nf-κB/MAPK signaling pathway in mice granulosa cells. Antioxidants (Basel). 2025;14:39.

21. Xie N, Zhang L, Gao W, Huang C, Huber PE, Zhou X, et al. NAD^+ metabolism: Pathophysiologic mechanisms and therapeutic potential. Signal Transduct Target Ther. 2020;5:227.

22. Liu K, Wei H, Nong W, Peng H, Li Y, Lei X, et al. Nampt/SIRT2/LDHA pathway-mediated lactate production regulates follicular dysplasia in polycystic ovary syndrome. Free Radic Biol Med. 2024;225:776–93.

23. Song S, Yang M, Li J, Li Y, Wang L, Yao S, et al. SIRT3 mediates CPT2 delactylation to enhance mitochondrial function and proliferation in goat granulosa cells. J Anim Sci Biotechnol. 2025;16:101.

24. Shi J, Zhao Z, Wang F, Zhao Y, Zhao Z, Xu D. Sirtuin 3 alleviates ovarian granulosa cell senescence through regulating mitochondrial quality control. Theriogenology. 2026;264:118054.

25. Yoshino J, Baur JA, Imai SI. NAD^+ intermediates: The biology and therapeutic potential of NMN and NR. Cell Metab. 2018;27:513–28.

26. Longo VD, Anderson RM. Nutrition, longevity and disease: From molecular mechanisms to interventions. Cell. 2022;185:1455–70.

27. Na X, Liu J, Tan Y, Meng L, Guo C, Zuo N, et al. Inhibiting TRIM21 neddylation rejuvenates oocyte quality in PCOS by regulating ubiquitination of CPT1A. Research (Wash D C). 2026;9:1223.

28. Tsai YR, Liao YN, Tsai CJ, Lee YA, Hsia SM, Lan KC, et al. Hyperandrogenism in polycystic ovary syndrome augments estrogen synthesis through AR-FOXL2-

576 mediated activation of the aromatase gene in granulosa cells. J Ovarian Res.
577 2025;18:200.
578 29. Wang L, Chen Y, Wei J, Guo F, Li L, Han Z, et al. Administration of nicotinamide
579 mononucleotide improves oocyte quality of obese mice. Cell Prolif. 2022;55:e13303.
580 30. Hao K, Chen F, Zhao L, Xu S, Xiong Y, Xu R, et al. Nicotinamide ameliorates
581 mitochondria-related neuronal apoptosis and cognitive impairment via the
582 NAD^+/SIRT3 pathway. Schizophrenia (Heidelb). 2023;9:32.
583 31. Beltra M, Pollanen N, Fornelli C, Tonttila K, Hsu MY, Zampieri S, et al. NAD^+
584 repletion with niacin counteracts cancer cachexia. Nat Commun. 2023;14:1849.
585 32. Escalante-Covarrubias Q, Mendoza-Viveros L, Gonzalez-Suarez M, Sitten-Olea R,
586 Velazquez-Villegas LA, Becerril-Perez F, et al. Time-of-day defines NAD^+ efficacy to
587 treat diet-induced metabolic disease by synchronizing the hepatic clock in mice. Nat
588 Commun. 2023;14:1685.
589 33. Huang L, Yao T, Chen J, Zhang Z, Yang W, Gao X, et al. Effect of Sirt3 on retinal
590 pigment epithelial cells in high glucose through Foxo3a/ PINK1-Parkin pathway
591 mediated mitophagy. Exp Eye Res. 2022;218:109015.
592 34. Yapryntseva MA, Maximchik PV, Zhivotovsky B, Gogvadze V. Mitochondrial
593 sirtuin 3 and various cell death modalities. Front Cell Dev Biol. 2022;10:947357.
594 35. Agarwal S, Muqit MMK. PTEN-induced kinase 1 (PINK1) and Parkin: Unlocking
595 a mitochondrial quality control pathway linked to Parkinson's disease. Curr Opin
596 Neurobiol. 2022;72:111–9.

36. Palikaras K, Lionaki E, Tavernarakis N. Mechanisms of mitophagy in cellular homeostasis, physiology and pathology. Nat Cell Biol. 2018;20:1013–22.

37. Jacobs DR, Jr., Gross MD, Tapsell LC. Food synergy: An operational concept for understanding nutrition. Am J Clin Nutr. 2009;89:1543S–8S.

38. Covarrubias AJ, Perrone R, Grozio A, Verdin E. NAD^+ metabolism and its roles in cellular processes during ageing. Nat Rev Mol Cell Biol. 2021;22:119–41.

39. Xian Y, Liu B, Shen T, Yang L, Peng R, Shen H, et al. Enhanced SIRT3 expression restores mitochondrial quality control mechanism to reverse osteogenic impairment in type 2 diabetes mellitus. Bone Res. 2025;13:30.

40. Mihanfar A, Nouri M, Roshangar L, Khadem-Ansari MH. Polyphenols: Natural compounds with promising potential in treating polycystic ovary syndrome. Reprod Biol. 2021;21:100500.

41. Almeida Balieiro CC, Hespanhol LC, Mendes Fonseca L, Wantowski S, Freitas MAA, Dias YJM, et al. Effects of polyphenol in women with polycystic ovary syndrome: A systematic review and meta-analysis of randomized controlled trials. Eur J Obstet Gynecol Reprod Biol. 2024;294:84–91.

42. Larik MO, Ahmed A, Khan L, Iftekhar MA. Effects of resveratrol on polycystic ovarian syndrome: A systematic review and meta-analysis of randomized controlled trials. Endocrine. 2024;83:51–9.

43. Tosatti JAG, Alves MT, Candido AL, Reis FM, Araujo VE, Gomes KB. Influence of n-3 fatty acid supplementation on inflammatory and oxidative stress markers in

patients with polycystic ovary syndrome: A systematic review and meta-analysis. Br J Nutr. 2021;125:657–68.

44. Zhang W, Zhang J, Xue H, Chen X, Li M, Chen S, et al. Nicotinamide mononucleotide improves endometrial homeostasis in a rat model of polycystic ovary syndrome by decreasing insulin resistance and regulating the glylytic pathway. Mol Nutr Food Res. 2024;68:e2400340.

45. Aflatounian A, Paris VR, Richani D, Edwards MC, Cochran BJ, Ledger WL, et al. Declining muscle NAD^+ in a hyperandrogenism PCOS mouse model: Possible role in metabolic dysregulation. Mol Metab. 2022;65:101583.

46. Fan Y, Hu Q, Wu X, Lang P, Wei Y, Yi R, et al. Reverse effects of nicotinamide mononucleotide supplementation on declining quality of oocytes with polycystic ovary syndrome. FASEB J. 2025;39:e70846.

47. Zhang Y, Huang K, Nong W, Guo Z, Xie Q, Lei X, et al. Nicotinamide mononucleotide attenuates hyperandrogenism in a polycystic ovary syndrome-like rat model by suppressing NLRP3 inflammasome-mediated granulosa-cell pyroptosis. J Ovarian Res. 2026;19:128.

Figure legends

Figure 1. Single-cell transcriptomic analysis reveals granulosa-cell heterogeneity and enrichment of NR0B1 target genes and insulin-response pathways in PMOS. Single-cell RNA-sequencing data from follicular-fluid-derived cells of three patients with PMOS and three healthy controls from the GSE240688 dataset were analyzed. (A) UMAP projection showing nine transcriptionally distinct cell clusters (clusters 0–8). (B) Dot plot showing the expression of representative cell-cycle- and p53-stress-related genes across clusters. Cluster 8 showed high expression of proliferation-associated genes, including MKI67 and PCNA, whereas cluster 5 exhibited a p53-stress-related transcriptional profile. Dot size indicates the proportion of cells expressing each gene, and color intensity represents the average expression level. (C) UMAP projection of annotated cell populations, including granulosa cell (GC), proliferating granulosa cell (cycle GC), p53-associated stress/arrest granulosa cell (p53-stop GC), neutrophils, dendritic cells, and monocyte/macrophage populations. (D) Dot plot of representative marker genes used for cell cluster annotation. Dot size indicates the proportion of cells expressing each gene, and color intensity represents the average expression level. (E) Venn diagram showing 14 genes shared between the NR0B1 target-gene set and the Gene Ontology biological process term “response to insulin”. (F) GSEA enrichment curves for the NR0B1 target-gene set and the insulin-response gene set based on GC pseudo-bulk expression profiles. (G) Normalized enrichment scores (NES) and corresponding P values for the two gene sets derived from GCs in patients with PMOS pseudo-bulk expression profiles: NR0B1 target-gene set, $P = 0.019$; insulin-response

gene set, $P = 0.039$.

Figure 2. DHT-induced PMOS mice display metabolic dysfunction and altered ovarian autophagy/mitophagy signaling. (A) Representative vaginal cytology images showing the characteristic cell morphology of proestrus (P), estrus (E), metestrus (M), and diestrus (D). (B) Glucose tolerance test (GTT) and insulin tolerance test (ITT) curves in control and PMOS mice after glucose or insulin administration, respectively (n = 5). (C) Quantification of the areas under the GTT and ITT curves (AUCs; n = 5). (D) Representative estrous-cycle profiles of control and PMOS mice monitored over 8 consecutive days. (E) Representative hematoxylin and eosin (H&E)-stained ovarian sections from control and PMOS mice. Ovaries from PMOS mice showed enlarged cystic follicles, thinning of the GC layer, and reduced corpus luteum formation (original magnification, × 10; scale bar, 50 μm). (F) Representative immunohistochemical images of Beclin1 and Pink1 in ovarian tissues from control and PMOS mice (original magnification, × 20; scale bar, 25 μm). (G) Quantification of Beclin1 and Pink1 immunostaining by average optical density (AOD; n = 3). (H) Western blot analysis of Pink1, p62, Parkin, LC3B-I, and LC3B-II protein expression in ovarian tissues, with HSP90 used as the loading control. (I) Densitometric quantification of Pink1, p62, Parkin, and LC3B-II protein expression normalized to HSP90 (n = 3). Data in (C), (G) and (I) were analyzed using two-tailed unpaired Student's t tests. $*P < 0.05$, $**P < 0.01$, $***P < 0.001$, $****P < 0.0001$.

Figure 3. PMOS is associated with elevated NAMPT expression, impaired NAD^+ homeostasis, and mitochondrial dysfunction in GCs. (A) Heatmap showing the standardized expression of representative genes associated with metabolism, insulin signaling, and nuclear-receptor regulation in pseudo-bulk GC expression profiles from patients with PMOS and healthy controls (n = 3 per group). NAMPT is highlighted by the red box, and the color scale indicates gene-wise standardized relative expression. (B) NAMPT immunohistochemical staining in ovarian sections obtained from control and PMOS mice (original magnification, × 20; scale bar, 25 μm). (C) Western blot analysis of NAMPT protein expression in ovarian tissues, with HSP90 used as the loading control. (D) Quantification of NAMPT immunostaining by average optical density. (E) RT-qPCR analysis of Nampt mRNA expression in ovarian tissues from control and PMOS mice. (F–H) Ovarian NAD^+ content, NADH content, and the NAD^+/NADH ratio in control and PMOS mice. (I) Western blot analysis of NAMPT protein expression in untreated control, vehicle-treated, and DHT-treated GCs, with HSP90 used as the loading control. (J) TOMM20 immunofluorescence in GCs subjected to control, NAMPT-knockdown, or NAMPT-overexpression conditions. Nuclei were counterstained with DAPI (original magnification, × 20; scale bar, 25 μm). (K) LC3 immunofluorescence in GCs from the indicated experimental groups. Nuclei were counterstained with DAPI (original magnification, × 20; scale bar, 25 μm). (L) Image-based measurements of TOMM20 fluorescence intensity and LC3-positive area (n = 3). (M) TMRE fluorescence demonstrating mitochondrial membrane potential under the indicated conditions. Nuclei were counterstained with Hoechst (original

magnification, × 20; scale bar, 25 μm). (N) MitoSOX Red fluorescence reflecting mitochondrial reactive oxygen species production in the indicated groups. Nuclei were counterstained with Hoechst (original magnification, × 20; scale bar, 25 μm). (O) Quantitative analysis of TMRE fluorescence and mitochondrial reactive oxygen species levels (n = 3). Values are shown as mean ± SD, with individual data points corresponding to independent experiments. Group differences were evaluated by one-way ANOVA with subsequent multiple-comparisons testing. *$P < 0.05$, **$P < 0.01$, ***$P < 0.001$, ****$P < 0.0001$.

Figure 4. NAMPT modulates SIRT3, whereas SIRT3 silencing disrupts mitochondrial homeostasis and alters mitophagy-related signaling in GCs. (A) Western blot analysis of NAMPT and SIRT3 protein expression in control, siRNA-negative-control, NAMPT-knockdown, and NAMPT-overexpression GCs, with HSP90 used as the loading control. (B) RT-qPCR analysis of NAMPT and SIRT3 mRNA expression in the indicated groups. (C) Western blot analysis of p62, Beclin1, NAMPT, LC3B-I, and LC3B-II protein expression in control, overexpression-negative-control, and NAMPT-overexpression GCs, with HSP90 used as the loading control. (D) Densitometric quantification of p62, Beclin1, and NAMPT protein expression and the LC3B-II/LC3B-I ratio. Protein expression was normalized to HSP90. (E) Western blot analysis of p62, Beclin1, Parkin, Pink1, SIRT3, LC3B-I, and LC3B-II protein expression in control, siRNA-negative-control, and SIRT3-knockdown GCs, with TUBULIN used as the loading control. (F) Densitometric quantification of p62, Beclin1, Parkin, Pink1, and

SIRT3 protein expression and the LC3B-II/LC3B-I ratio. Protein expression was normalized to TUBULIN. (G) TOMM20 fluorescence patterns in GCs subjected to the indicated treatments (original magnification, × 20; scale bar, 25 μm). (H) LC3 fluorescence distribution under the corresponding experimental conditions (original magnification, × 20; scale bar, 25 μm). (I) Quantitative assessment of TOMM20 fluorescence intensity and LC3-positive area. (J)TMRE fluorescence profiles illustrating changes in mitochondrial membrane potential. Nuclei were counterstained with Hoechst (original magnification, × 20; scale bar, 25 μm). (K) MitoSOX Red fluorescence reflecting mitochondrial reactive oxygen species accumulation. Nuclei were counterstained with Hoechst (original magnification, × 20; scale bar, 25 μm). (L) Quantitative comparison of TMRE fluorescence and mitochondrial reactive oxygen species levels.Results are expressed as mean ± SD; each symbol denotes one independent experiment (n = 3). Group differences were tested by one-way ANOVA followed by multiple-comparisons testing. *$P < 0.05$, **$P < 0.01$, ***$P < 0.001$, ****$P < 0.0001$.

Figure 5. NMN restores the NAD^+/SIRT3 axis and ameliorates mitochondrial dysfunction in the cell model of PMOS. (A–C) Intracellular NAD^+ content, NADH content, and the NAD^+/NADH ratio in control, NAMPT-knockdown, and NAMPT-knockdown plus NMN-treated GCs (n = 3). (D) Western blot analysis of NAMPT, Parkin, Pink1, LC3B-I, and LC3B-II protein expression in control, siRNA-negative-control, si-NAMPT (75nM), si-NAMPT (100nM), si-NAMPT (100nM) plus NMN, and

NMN-treated GCs, with HSP90 used as the loading control. (E–H) Densitometric quantification of NAMPT, Parkin, and Pink1 protein expression and the LC3B-II/LC3B-I ratio. NAMPT, Parkin, and Pink1 protein expression was normalized to HSP90 (n = 3). NMN restores SIRT3 expression and attenuates DHT-induced mitochondrial dysfunction and mitophagy-related abnormalities in GCs. (I) Western blot analysis of SIRT3 protein expression in untreated control, vehicle-treated, DHT-treated, and DHT plus NMN-treated GCs, with HSP90 used as the loading control. (J, K) RT-qPCR analysis of SIRT3 and SOD2 mRNA expression in the indicated groups. (L) TOMM20 fluorescence following NAMPT knockdown with or without NMN treatment. Nuclei were counterstained with DAPI (original magnification, × 20; scale bar, 25 μm). (M) LC3 fluorescence in the corresponding treatment groups. Nuclei were counterstained with DAPI (original magnification, × 20; scale bar, 25 μm). (N) Quantification of relative TOMM20 fluorescence intensity and LC3-positive area (n = 3). (O) Changes in mitochondrial membrane potential visualized by TMRE fluorescence. Nuclei were counterstained with Hoechst (original magnification, × 20; scale bar, 25 μm). (P) Mitochondrial reactive oxygen species visualized using MitoSOX Red. Nuclei were counterstained with Hoechst (original magnification, × 20; scale bar, 25 μm). (Q) Quantitative analysis of TMRE fluorescence intensity and mitochondrial reactive oxygen species levels (n = 3). Data represent mean ± SD from three independent experiments. Statistical differences among groups were determined using one-way ANOVA followed by multiple-comparisons testing. $*P < 0.05$, $**P < 0.01$, $***P < 0.001$, $****P < 0.0001$.

Figure 6. NMN ameliorates metabolic and ovarian abnormalities in DHT-induced PMOS mice and modulates ovarian NAD^+/NADH homeostasis and autophagy/mitophagy-related signaling. (A) Schematic overview of the experimental design. After acclimatization, female C57BL/6J mice were randomly assigned to the control, PMOS, and PMOS plus NMN groups. PMOS was induced with DHT, and NMN was administered for 21 consecutive days. Estrous-cycle monitoring, glucose tolerance tests (GTTs), insulin tolerance tests (ITTs), serum hormone measurements, and ovarian tissue analyses were subsequently performed. (B, C) ITT curves and corresponding areas under the curve (AUCs) in control, PMOS, and PMOS plus NMN mice (n = 8, 5, and 5 mice, respectively). (D, E) GTT curves and corresponding AUCs in the indicated groups (n = 8, 5, and 5 mice for the control, PMOS, and PMOS plus NMN groups, respectively). (F) Representative hematoxylin and eosin (H&E)-stained ovarian sections from PMOS and PMOS plus NMN mice (original magnification, × 10; scale bar, 50 μm). (G) Representative estrous-cycle profiles of control, PMOS, and PMOS plus NMN mice monitored over 8 consecutive days. (H) Serum luteinizing hormone (LH), follicle-stimulating hormone (FSH), LH/FSH ratio, and testosterone levels in the indicated groups (n = 9 mice/group). (I) Ovarian NAD^+ content, NADH content, and the NAD^+/NADH ratio in the indicated groups (n = 3 mice/group). (J) Representative immunohistochemical images of Beclin1 and Pink1 in ovarian tissues from PMOS and PMOS plus NMN mice (original magnification, × 20; scale bar, 25 μm). (K) Quantification of Beclin1 and Pink1 immunostaining by average optical

794 density (AOD) (n = 3 mice/group). (L) Western blot analysis of p62, Beclin1, NAMPT,
795 Parkin, Pink1, SIRT3, LC3B-I, and LC3B-II protein expression in ovarian tissues, with
796 TUBULIN used as the loading control. (M) Quantification of RT-qPCR results for p62,
797 Beclin1, Nampt, Parkin, Pink1, Sirt3, and LC3B mRNA expression (n = 3 mice/group).
798 Comparisons among groups were performed using one-way ANOVA followed by
799 multiple-comparisons testing. Data in (K) were analyzed using two-tailed unpaired
800 Student's t tests. *$P < 0.05$, **$P < 0.01$, ***$P < 0.001$, and ****$P < 0.0001$.

Fig 1

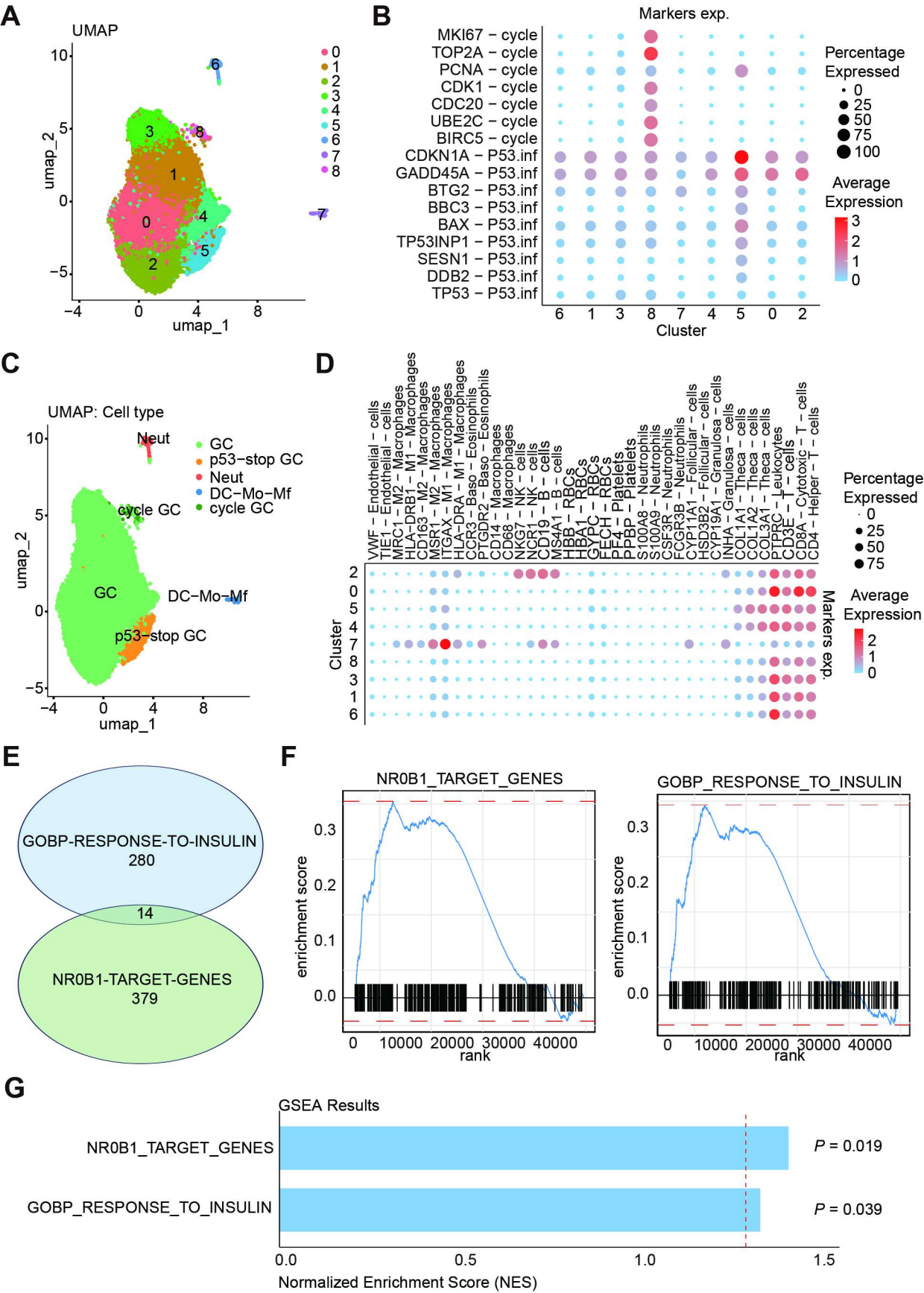

A
UMAP
umap_2
umap_1
0
1
2
3
4
5
6
7
8
B
Markers exp.
MKI67 – cycle
TOP2A – cycle
PCNA – cycle
CDK1 – cycle
CDC20 – cycle
UBE2C – cycle
BIRC5 – cycle
CDKN1A – P53.inf
GADD45A – P53.inf
BTG2 – P53.inf
BBC3 – P53.inf
BAX – P53.inf
TP53INP1 – P53.inf
SESN1 – P53.inf
DDB2 – P53.inf
TP53 – P53.inf
6 1 3 8 7 4 5 0 2
Cluster
Percentage Expressed
0
25
50
75
100
Average Expression
3
2
1
0
C
UMAP: Cell type
Neut
GC
p53−stop GC
Neut
DC−Mo−Mf
cycle GC
cycle GC
GC
DC−Mo−Mf
p53−stop GC
umap_2
umap_1
D
VWF – Endothelial – cells
TIE1 – Endothelial – cells
MRC1 – M2 – Macrophages
HLA−DRB1 – M1 – Macrophages
CD163 – M2 – Macrophages
MSR1 – M2 – Macrophages
ITGAX – M1 – Macrophages
HLA−DRA – M1 – Macrophages
CCR3 – Baso – Eosinophils
PTGDR2 – Baso – Eosinophils
CD14 – Macrophages
CD68 – Macrophages
NKG7 – NK – cells
NCR1 – NK – cells
CD19 – B – cells
MS4A1 – B – cells
HBB – RBCs
HBA1 – RBCs
GYPC – RBCs
FECH – RBCs
PF4 – Platelets
PPBP – Platelets
S100A8 – Neutrophils
S100A9 – Neutrophils
CSF3R – Neutrophils
FCGR3B – Neutrophils
CYP11A1 – Follicular – cells
HSD3B2 – Follicular – cells
CYP19A1 – Granulosa – cells
INHA – Granulosa – cells
COL1A1 – Theca – cells
COL1A2 – Theca – cells
COL3A1 – Theca – cells
PTPRC – Leukocytes
CD3E – T – cells
CD8A – Cytotoxic – T – cells
CD4 – Helper – T – cells
Cluster
2 0 5 4 7 8 3 1 6
Markers exp.
Percentage Expressed
0
25
50
75
Average Expression
2
1
0
E
GOBP-RESPONSE-TO-INSULIN
280
14
NR0B1-TARGET-GENES
379
F
NR0B1_TARGET_GENES
GOBP_RESPONSE_TO_INSULIN
enrichment score
0.0
0.1
0.2
0.3
0
10000
20000
30000
40000
rank
G
GSEA Results
NR0B1_TARGET_GENES
GOBP_RESPONSE_TO_INSULIN
P = 0.019
P = 0.039
0.0
0.5
1.0
1.5
Normalized Enrichment Score (NES)

Fig 2

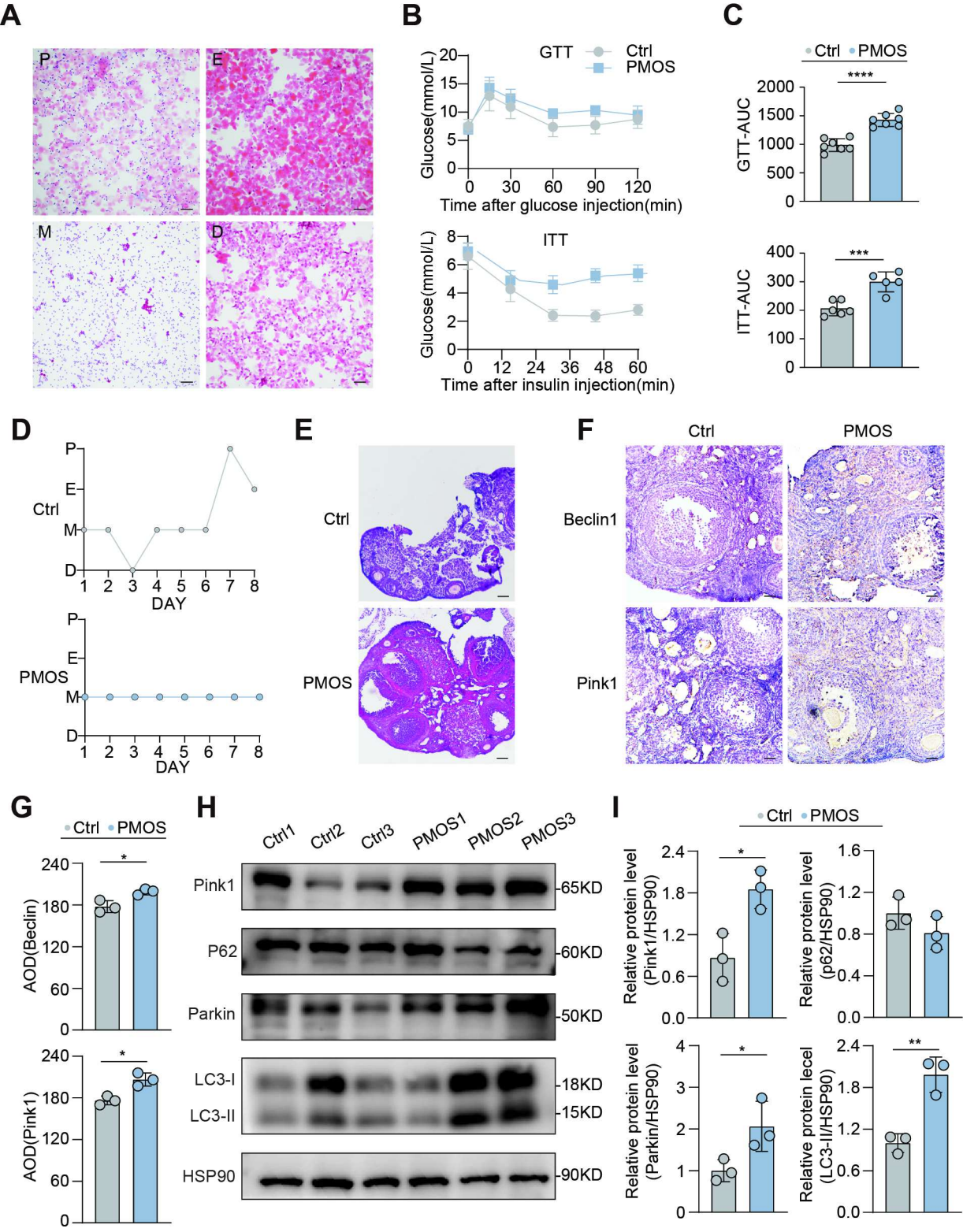

A
P
E
M
D
B
GTT
Ctrl
PMOS
Glucose(mmol/L)
Time after glucose injection(min)
ITT
Glucose(mmol/L)
Time after insulin injection(min)
C
Ctrl
PMOS
GTT-AUC
ITT-AUC
D
Ctrl
PMOS
DAY
E
Ctrl
PMOS
F
Ctrl
PMOS
Beclin1
Pink1
G
Ctrl
PMOS
AOD(Beclin)
AOD(Pink1)
H
Ctrl1
Ctrl2
Ctrl3
PMOS1
PMOS2
PMOS3
Pink1
P62
Parkin
LC3-I
LC3-II
HSP90
65KD
60KD
50KD
18KD
15KD
90KD
I
Ctrl
PMOS
Relative protein level (Pink1/HSP90)
Relative protein level (p62/HSP90)
Relative protein level (Parkin/HSP90)
Relative protein lecel (LC3-II/HSP90)

Fig 3

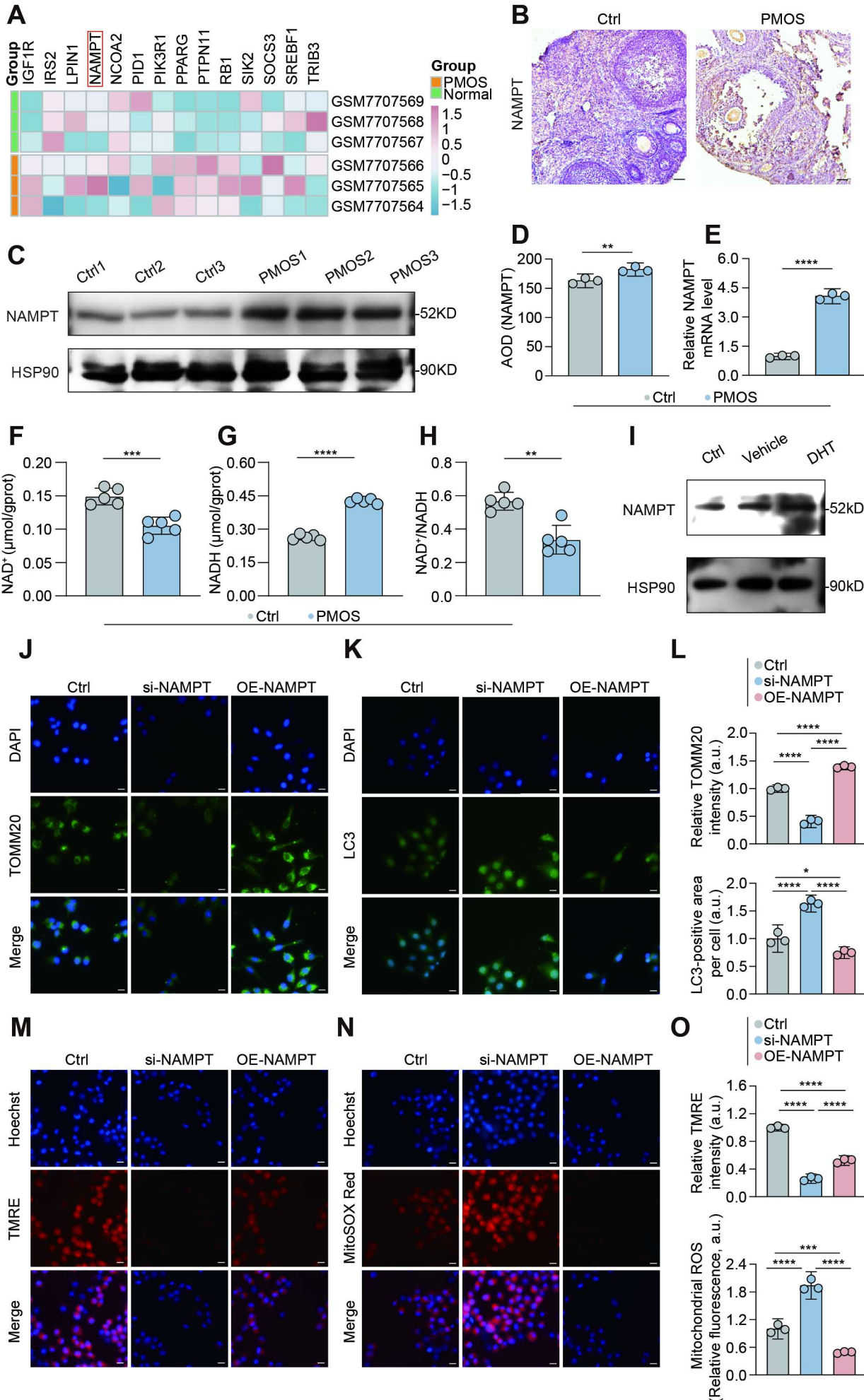

A
Group
IGF1R
IRS2
LPIN1
NAMPT
NCOA2
PID1
PIK3R1
PPARG
PTPN11
RB1
SIK2
SOCS3
SREBF1
TRIB3
GSM7707569
GSM7707568
GSM7707567
GSM7707566
GSM7707565
GSM7707564
Group
PMOS
Normal
1.5
1
0.5
0
−0.5
−1
−1.5
B
Ctrl
PMOS
NAMPT
C
Ctrl1
Ctrl2
Ctrl3
PMOS1
PMOS2
PMOS3
NAMPT
52KD
HSP90
90KD
D
AOD (NAMPT)
200
150
100
50
0
**
Ctrl
PMOS
E
Relative NAMPT mRNA level
6.0
4.5
3.0
1.5
0.0
****
Ctrl
PMOS
F
NAD+ (μmol/gprot)
0.20
0.15
0.10
0.05
0.00
***
G
NADH (μmol/gprot)
0.60
0.45
0.30
0.15
0.00
****
H
NAD+/NADH
0.8
0.6
0.4
0.2
0.0
**
Ctrl
PMOS
I
Ctrl
Vehicle
DHT
NAMPT
52kD
HSP90
90kD
J
Ctrl
si-NAMPT
OE-NAMPT
DAPI
TOMM20
Merge
K
Ctrl
si-NAMPT
OE-NAMPT
DAPI
LC3
Merge
L
Ctrl
si-NAMPT
OE-NAMPT
Relative TOMM20 intensity (a.u.)
2.0
1.5
1.0
0.5
0.0
****
****
****
LC3-positive area per cell (a.u.)
2.0
1.5
1.0
0.5
0.0
*
****
****
M
Ctrl
si-NAMPT
OE-NAMPT
Hoechst
TMRE
Merge
N
Ctrl
si-NAMPT
OE-NAMPT
Hoechst
MitoSOX Red
Merge
O
Ctrl
si-NAMPT
OE-NAMPT
Relative TMRE intensity (a.u.)
1.6
1.2
0.8
0.4
0.0
****
****
****
Mitochondrial ROS (Relative fluorescence, a.u.)
2.4
1.8
1.2
0.6
0.0
***
****
****

Fig 4

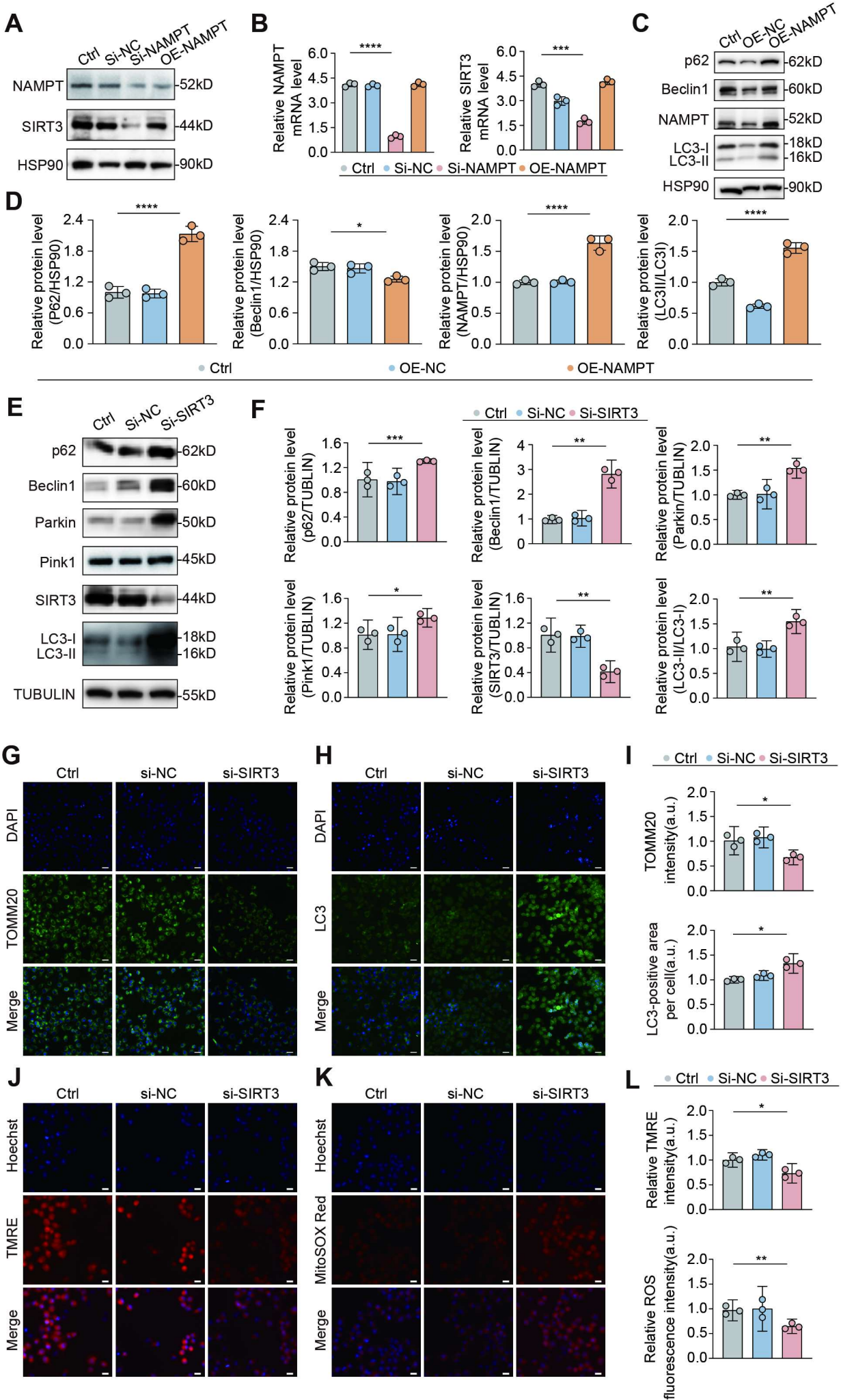

A
Ctrl
Si-NC
Si-NAMPT
OE-NAMPT
NAMPT
SIRT3
HSP90
52kD
44kD
90kD
B
Relative NAMPT mRNA level
Relative SIRT3 mRNA level
****
***
Ctrl
Si-NC
Si-NAMPT
OE-NAMPT
C
Ctrl
OE-NC
OE-NAMPT
p62
Beclin1
NAMPT
LC3-I
LC3-II
HSP90
62kD
60kD
52kD
18kD
16kD
90kD
D
Relative protein level (P62/HSP90)
Relative protein level (Beclin1/HSP90)
Relative protein level (NAMPT/HSP90)
Relative protein level (LC3II/LC3I)
Ctrl
OE-NC
OE-NAMPT
E
Ctrl
Si-NC
Si-SIRT3
p62
Beclin1
Parkin
Pink1
SIRT3
LC3-I
LC3-II
TUBULIN
62kD
60kD
50kD
45kD
44kD
18kD
16kD
55kD
F
Ctrl
Si-NC
Si-SIRT3
Relative protein level (p62/TUBLIN)
Relative protein level (Beclin1/TUBLIN)
Relative protein level (Parkin/TUBLIN)
Relative protein level (Pink1/TUBLIN)
Relative protein level (SIRT3/TUBLIN)
Relative protein level (LC3-II/LC3-I)
G
Ctrl
si-NC
si-SIRT3
DAPI
TOMM20
Merge
H
Ctrl
si-NC
si-SIRT3
DAPI
LC3
Merge
I
Ctrl
Si-NC
Si-SIRT3
TOMM20 intensity(a.u.)
LC3-positive area per cell(a.u.)
J
Ctrl
si-NC
si-SIRT3
Hoechst
TMRE
Merge
K
Ctrl
si-NC
si-SIRT3
Hoechst
MitoSOX Red
Merge
L
Ctrl
Si-NC
Si-SIRT3
Relative TMRE intensity(a.u.)
Relative ROS fluorescence intensity(a.u.)

Fig 5

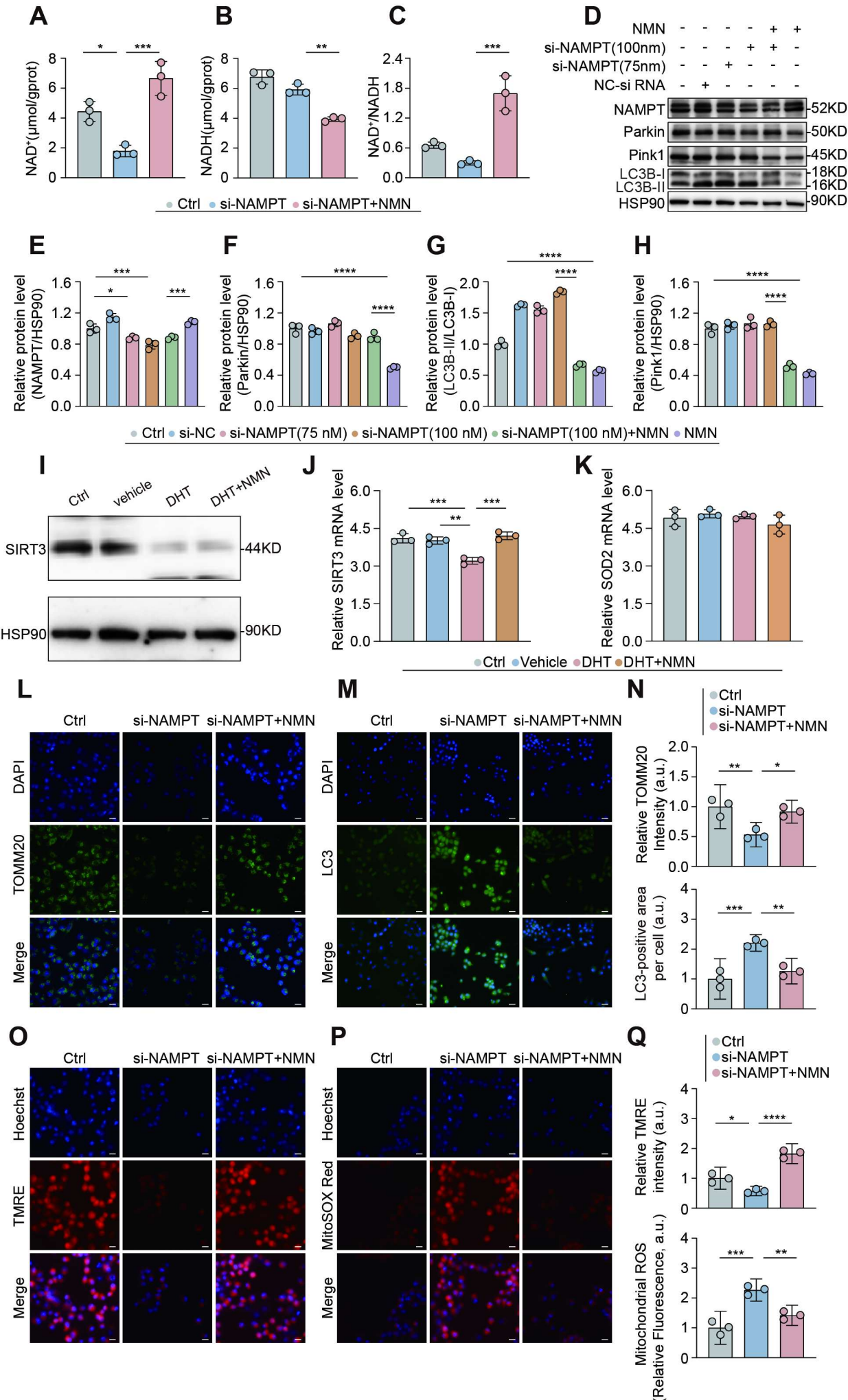
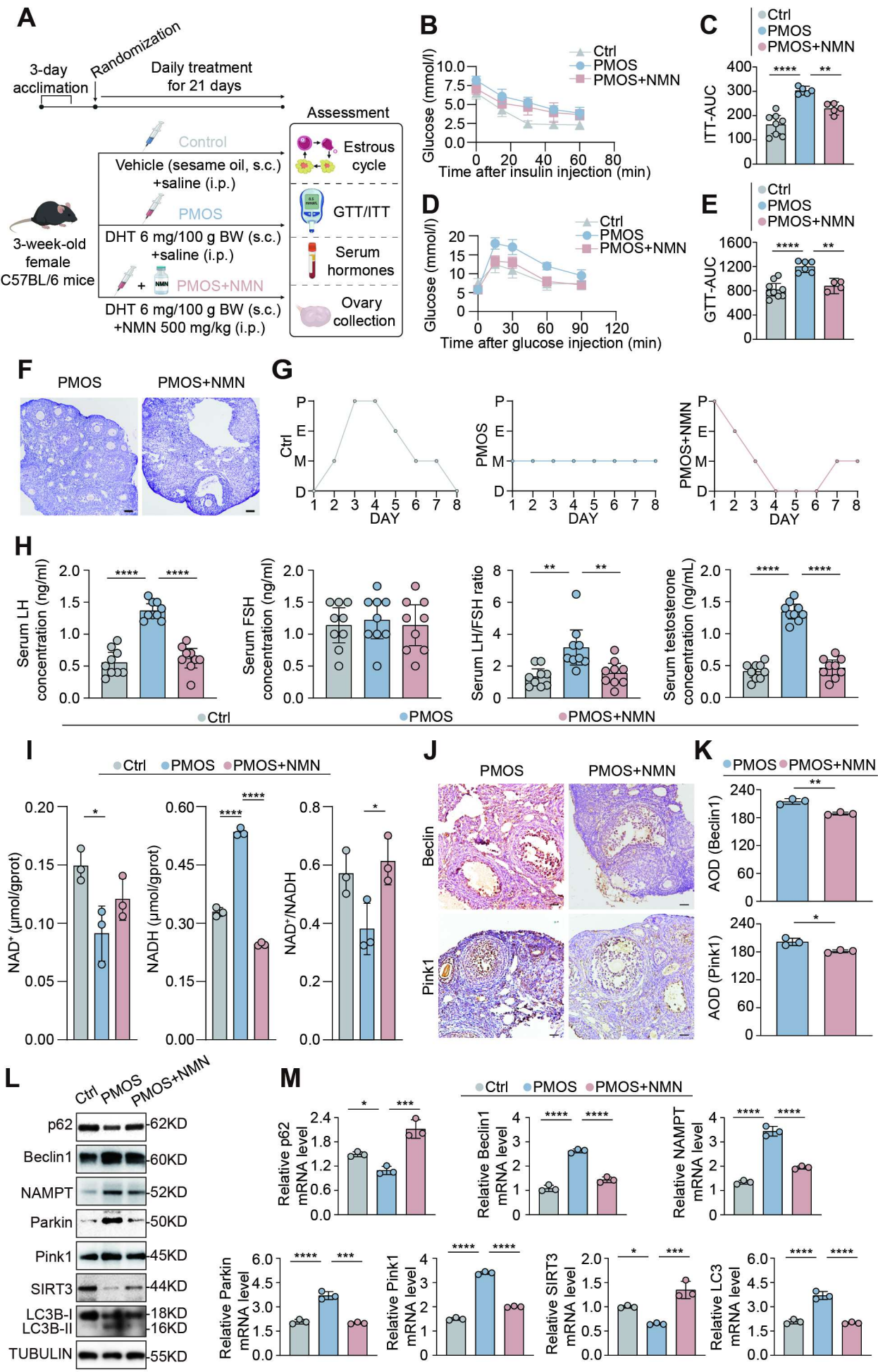

A
B
C
D
NAD+(μmol/gprot)
NADH(μmol/gprot)
NAD+/NADH
Ctrl
si-NAMPT
si-NAMPT+NMN
NMN
si-NAMPT(100nm)
si-NAMPT(75nm)
NC-si RNA
NAMPT
Parkin
Pink1
LC3B-I
LC3B-II
HSP90
52KD
50KD
45KD
18KD
16KD
90KD
E
F
G
H
Relative protein level (NAMPT/HSP90)
Relative protein level (Parkin/HSP90)
Relative protein level (LC3B-II/LC3B-I)
Relative protein level (Pink1/HSP90)
Ctrl
si-NC
si-NAMPT(75 nM)
si-NAMPT(100 nM)
si-NAMPT(100 nM)+NMN
NMN
I
J
K
Ctrl
vehicle
DHT
DHT+NMN
SIRT3
HSP90
44KD
90KD
Relative SIRT3 mRNA level
Relative SOD2 mRNA level
Ctrl
Vehicle
DHT
DHT+NMN
L
M
N
Ctrl
si-NAMPT
si-NAMPT+NMN
DAPI
TOMM20
Merge
LC3
Relative TOMM20 Intensity (a.u.)
LC3-positive area per cell (a.u.)
O
P
Q
Hoechst
TMRE
MitoSOX Red
Relative TMRE intensity (a.u.)
Mitochondrial ROS (Relative Fluorescence, a.u.)

Fig 6


A
3-day acclimation
Randomization
Daily treatment for 21 days
Control
Vehicle (sesame oil, s.c.) +saline (i.p.)
PMOS
DHT 6 mg/100 g BW (s.c.) +saline (i.p.)
PMOS+NMN
DHT 6 mg/100 g BW (s.c.) +NMN 500 mg/kg (i.p.)
3-week-old female C57BL/6 mice
Assessment
Estrous cycle
GTT/ITT
Serum hormones
Ovary collection
B
Glucose (mmol/l)
Time after insulin injection (min)
Ctrl
PMOS
PMOS+NMN
C
ITT-AUC
D
Glucose (mmol/l)
Time after glucose injection (min)
E
GTT-AUC
F
PMOS
PMOS+NMN
G
Ctrl
PMOS
PMOS+NMN
P
E
M
D
DAY
H
Serum LH concentration (ng/ml)
Serum FSH concentration (ng/ml)
Serum LH/FSH ratio
Serum testosterone concentration (ng/mL)
I
NAD⁺ (μmol/gprot)
NADH (μmol/gprot)
NAD⁺/NADH
J
PMOS
PMOS+NMN
Beclin
Pink1
K
AOD (Beclin1)
AOD (Pink1)
L
Ctrl
PMOS
PMOS+NMN
p62
Beclin1
NAMPT
Parkin
Pink1
SIRT3
LC3B-I
LC3B-II
TUBULIN
62KD
60KD
52KD
50KD
45KD
44KD
18KD
16KD
55KD
M
Relative p62 mRNA level
Relative Beclin1 mRNA level
Relative NAMPT mRNA level
Relative Parkin mRNA level
Relative Pink1 mRNA level
Relative SIRT3 mRNA level
Relative LC3 mRNA level

Supplementary Files

This is a list of supplementary files associated with this preprint. Click to download.

- SupplementaryInformation.docx